Investigation into a suitable scintillator and coded-aperture material for a mixed-field radiation imaging system

Published by IOP Publishing for Sissa Medialab

Received: *October 9, 2017*
Accepted: *November 12, 2017*
Published: *December 6, 2017*

Investigation into a suitable scintillator and coded-aperture material for a mixed-field radiation imaging system

M.J. Cieślak,[a,1] **K.A.A. Gamage**[b] **and R. Glover**[c]

[a] *Department of Engineering, Lancaster University, Lancaster LA1 4YW, U.K.*
[b] *School of Engineering, University of Glasgow, Glasgow, G12 8QQ, U.K.*
[c] *Radiometric Systems Group, Sellafield Ltd, Seascale CA20 1PG, U.K.*

E-mail: m.cieslak@lancaster.ac.uk

Abstract: Monte-Carlo modelling (MCNPX) methods have been employed to conduct an investigation into a suitable scintillator and coded-aperture material for a scintillator based mixed-field radiation imaging system. Single stilbene crystal, pure and ^{6}Li-loaded plastic scintillators were simulated and their neutron/gamma detection performance compared when exposed to the spontaneous fission spectrum produced by ^{252}Cf. The most suitable candidate was then incorporated into a scintillator based mixed-field coded-aperture imaging system. Coded-aperture models made of three W and ^{113}Cd compositions were tested in different neutron/gamma environments with a square W collimator modelled around the aperture. Each simulation involved recording the interactions of neutron events in organic solid scintillator, whose neutron/gamma detection performance was assessed prior to the coded-aperture material investigation. Three coded-aperture material compositions have been tested with the simulated ^{252}Cf spontaneous fission as well as ^{241}AmBe neutron sources. Results generally claim very good detection sensitivity and spatial resolution for the radioactive sources located in the centre of the aperture.

Keywords: Instrumentation for neutron sources; Neutron detectors (cold, thermal, fast neutrons); Radiation monitoring; Scintillators, scintillation and light emission processes (solid, gas and liquid scintillators)

[1]Corresponding author.

https://doi.org/10.1088/1748-0221/12/12/P12007

2017 JINST 12 P12007

Contents

2017 JINST 12 P12007

1 Introduction

1.1 Scintillator detector

Over the years, organic liquid scintillators have become the preferred choice for neutron detection and imaging instruments [1–4]. Although organic liquid scintillators are sensitive to both neutrons and gamma-ray photons, the difference in the fluorescence decay rate of heavily-ionising particles such as protons (resulting from neutron interactions) and electrons (resulting from gamma-ray photons interactions) can be utilised to infer the origin of the interaction [5]. As such, organic liquid scintillators provide a viable solution for mixed-field characterisation, when pulse-shape discrimination (PSD) methods are employed to reliably separate neutron events from gamma-ray interactions within the organic liquid scintillator [6].

Properties of some organic liquid scintillators, such as low flashpoint and susceptibility to leaks, make them unsuitable for certain industrial applications. However, the same discrimination methods can be exploited to separate particles within less flammable and less hazardous organic solid scintillators [7, 8]. Owing to continuous development, organic plastics and crystals have shown a significant improvement in their PSD capabilities in recent years. While plastics currently remain inferior to their liquid counterparts, solution-grown stilbene crystal claims better PSD performance in comparison to one of the most widely used organic liquid scintillator EJ-309 [9, 10].

In this study, a scintillation material suitable for mixed-field characterisation in nuclear decommissioning applications was sought. Due to the safety concerns related to the nuclear decommissioning sites low flammability and non-hazardous nature of the sensitive detectors were required.

Thus, only organic plastic and crystal scintillators were investigated. Pure plastic, ^{6}Li-loaded plastic and single stilbene crystal scintillation samples were tested within a simulated spontaneous fission spectrum of heavily shielded ^{252}Cf. Perfect neutron/gamma PSD was assumed, and the three samples comparison performed based on the neutron/photon flux recorded within the scintillator as well as number of neutron and photon interactions within each scintillator sample based on PTRAC card implementation in MCNPX. MCNPX version 2.7.0 was utilised to perform all the simulations described in this paper [11].

1.2 Coded-aperture material

Many of the mixed-field characterisation systems utilise a sensitive detector in a form of an organic scintillator [6, 12–14]. These can be found in collimated single pinhole cameras utilised in many branches of nuclear instrumentation engineering to facilitate radiation imaging requirements. Despite their limitations, primarily related to the interdependence between spatial resolution and signal to noise ratio (SNR), collimator based radiation imaging systems have been successfully implemented in gamma-ray and neutron imaging systems [2, 15–17]. Development of multi-hole cameras with aperture patterns based on uniformly redundant arrays (URAs) and modified URAs (MURAs) allowed the development of high resolution radiation cameras without affecting SNR [18, 19]. Consequently, coded-aperture imaging (CAI) was favourably adopted in X- and gamma-ray localisation applications [20, 21]. Authors' previous work presents a detailed review of CAI systems [22].

Research into coded-aperture based neutron imaging system has been recently revived due to continuous development of the PSD capable organic scintillators and the advancements in digital signal processing on Field Programmable Gate Arrays (FPGAs). The difficulty arises, when PSD is required to be performed simultaneously on multiple channels, which is the case for scintillator based coded-aperture neutron imaging systems (CANIS). Moreover, CANIS requires image reconstruction to be performed, once PSD is completed. Reconstruction algorithm does not only increase the computational overhead, but also requires that the incoming particles are effectively prevented, via coded-aperture's opaque elements, from reaching the sensitive detector.

It follows that the coded-aperture material must be carefully chosen, so that the likelihood of misclassification of the particles reaching the elements of the sensitive detector is reduced to minimum. Owing to the characteristics of neutron interactions with matter, detectors tend to be focused on a specific energy range, such as thermal or fast neutron systems. Systems targeting fast neutron detection can utilise either *active* or *passive* coded-aperture system.

Active CAI is performed, when the aperture is built of neutron detectors and double scattering (in the aperture and the sensitive detector) is utilised to infer the time-of-flight and the direction of the incident neutron [23]. *Passive* CAI relies either on the high neutron absorption cross-section materials, such as polyethylene, or neutron reflecting materials, such as natural W. In contrast to the *active* coded-aperture approach, neutron interaction within the aperture is not directly used to perform localisation [24].

The most advanced example of the application of CAI techniques into neutron imaging and localisation has been presented by Hausladen et al. [25]. This scintillator based CANIS is aimed at fast neutron detection and utilises rank-11 MURA design for the coded-aperture, which was built from high-density polyethylene (HDPE) to modulate the fast neutron field. The most recent implementation of the work reports on the use of an array of sensitive detectors built of the EJ-299-34

2017 JINST 12 P12007

plastic scintillators [26]. Each scintillator element has a PMT attached to it, which allows for an easy localisation of the particle interaction. Experiments performed with multiple neutron sources of similar strength present reasonable localisation accuracy, without the need for complicated analysis.

Based on author's preceding work, in this paper, MCNPX code was used to investigate the suitability of three W-^{113}Cd compositions for a portable scintillator based coded-aperture neutron imaging system. Each material was examined with ^{252}Cf and ^{241}AmBe radiation sources to observe its behaviour in different environments with varied neutron energy spectra. In each case neutron and photon energy spectra were manually defined for the sources specified. As a result, the potential of simultaneous neutron and gamma-ray sources identification was examined. In contrast to the aforementioned CANISs an array of small scintillation detector bars was constructed, whose each detector bar is to be linked to a single pixel of H9500 Hamamatsu MAMPT [27], in order to infer the location of the interaction.

2 Simulation based comparison of solid organic scintillators

2.1 Geometry and physics

Real-life experimental scenario geometry — as available at Lancaster University, Lancaster, U.K. — has been used for the simulation based investigation performed in this study. Spontaneous fission source ^{252}Cf of 2.65 years half-life and average neutron energy spectrum of 2.1 MeV is stored in the centre of a water-filled metal tank. During experiments the source is pneumatically released and moved towards the edge of the side of the tank (for the purposes of this simulation based study the source is retained in the released position). Detectors are normally placed in closed vicinity to the edge of the tank as shown in figure 1. There is also a 5 cm thick Pb block placed adjacent to the tank in order to reduce the number of gamma-ray photons reaching the sensitive detector. Similar approach has been previously adopted by Zaitseva et al. [8], where 5.1 cm of Pb reduced the number of gamma-ray photons to the same number as neutrons.

Fast neutrons are most likely to undergo elastic scattering with a proton, as a result of an interaction with nuclei in matter. In a similar way, gamma-ray photons will interact with the organic scintillant through Compton scattering with an electron [28]. These neutron and photon collisions in matter were examined for three different organic scintillation detectors. Mixed-field detector assembly comprising cylindrical scintillator sample and a PMT enclosed in an aluminium housing was placed 15 cm away from the side of the tank, where the radiation source is located during experiments.

For the purposes of the simulation work carried out in this study, neutron energy spectrum was defined using Watt fission spectrum. Gamma spectrum was defined based on the information presented by Valentine [29] and Gehrke et al. [30]. Energy spectra of both neutron and gamma-ray photons yielded by the unshielded ^{252}Cf were recorded in MCNPX using a small volume (cylindrical) stilbene detector. These are used for reference, and are contrasted with the flux measurement at the location within the experimental geometry, where the scintillator samples were later placed. Particle flux measurements, as shown in figure 2, illustrate the scale of moderation provided by the water tank where the source is normally kept.

Solid plastic scintillator sample was modelled based on the information provided in EJ-299-33/34 data sheet from Eljen Technology [26]. In a similar way, single stilbene crystal was modelled

2017 JINST 12 P12007

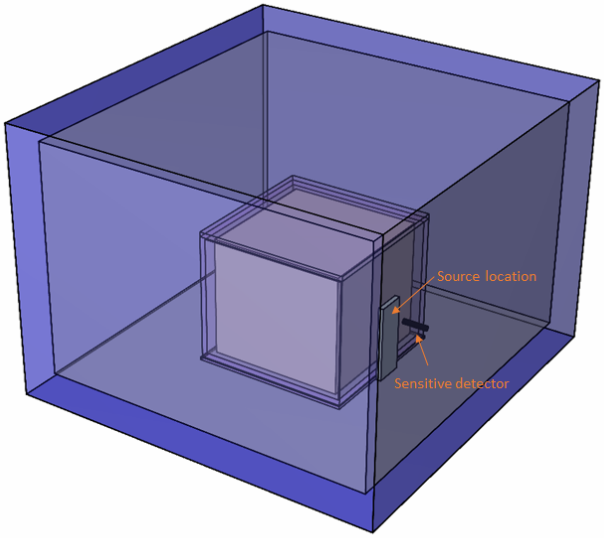

Figure 1. Geometry of the water-filled metal tank, where the ^{252}Cf fission source is kept at Lancaster University. Orange arrows point to the source location, when it is released for experiments, and to the placement of the sensitive detector.

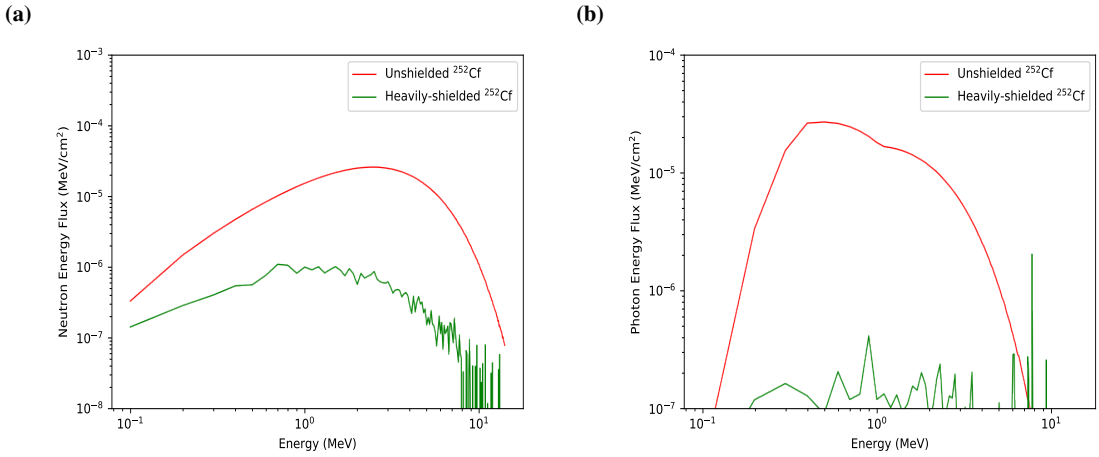

Figure 2. Unshielded and heavily-shielded (by means of water) particle energy spectra of ^{252}Cf for: a) neutrons and b) gamma-ray photons.

using the information provided by Inrad Optics [31], whereas ^{6}Li-loaded plastic scintillator was modelled based on the data obtained from Balmer et al. [32]. Each scintillator sample, placed in a cylindrical Al enclosure, was in turn irradiated with the ^{252}Cf source. Walls surrounding the water tank were built of concrete completing the model of the neutron laboratory. The laboratory was filled with air to resemble the factual experimental environment.

2017 JINST 12 P12007

3 Coded-aperture optimisation

3.1 Geometry and physics

Based on the authors' preceding work, coded-aperture model examined in this work, was rank-7 MURA design. Detailed description of the design process and initial feasibility study can be found here [22]. It is worth noticing at this point that there is a correlation between the rank of the aperture and the resolution of the reconstructed image. Generally, the resolution increases with the growing rank of the aperture. However, higher rank apertures can be difficult to manufacture in materials, such as W and ^{113}Cd, due to fragility of very small elements. Moreover, it is the thickness of the aperture that contributes in a greater way to the performance of the imaging system, as shown by Gmar et al. [33], when the aperture is required to successfully block the incoming particles in the opaque elements.

Due to neutron source localisation issues identified in the initial work, a square collimator was added to the original design, aiming to prevent particles from escaping the geometry around the aperture. The new geometry is presented in figure 3. Further, gamma-ray photon spectrum was added in order to reflect the real-life scenario more closely. The dimensions of a single aperture cell, as well as the dimensions of an individual detector cell were adjusted to the dimensions of a single anode of Hamamatsu's H9500 MAPMT.

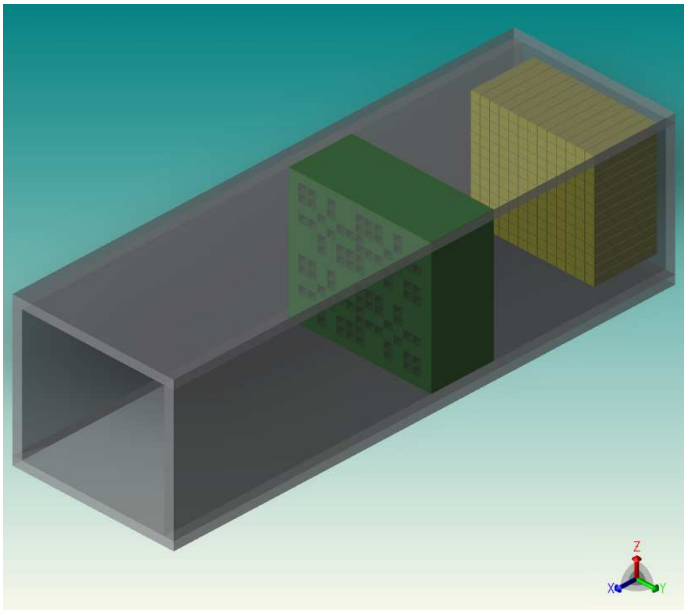

Figure 3. Geometry modelled in SuperMC was translated to MCNPX particle transport code [34]. Collimator is shown in grey, coded-aperture in green and sensitive detector in yellow.

The coded-aperture model — shown in green in figure 3 — was in turn exposed to ^{252}Cf (spontaneous fission) and ^{241}AmBe neutron source. In each case, the radiation source was located 18 cm away from the aperture front. The sensitive detector thickness was set to 15 mm and was placed 50 mm behind the aperture; 10 mm thick square collimator encloses the modelled set-up as presented in figure 3. Geometry presented in figure 3 is a not to scale representation of the testing environment generated in SuperMC software. Properties such as thickness and materials were then

2017 JINST 12 P12007

manually adjusted to a specific simulation scenario in MCNPX input files. The presented MCNPX geometry was placed in an air-filled sphere.

Single stilbene crystal showed a very good neutron detection performance, when tested with neutron spectrum of ^{252}Cf in the previous study [22]. Its neutron/gamma detection performance was further investigated in the first part of this work. It also presents best neutron/gamma sensitivity out the three samples tested as evidenced by the results presented in section 4 of this paper. Thus, single stilbene crystal was used to build the pixelated sensitive detector, as represented in yellow in figure 3.

With the various radiation sources placed in turn 18 cm away from the aperture front neutron and gamma-ray photon fluxes, as well as energy deposited in the individual sensitive detector cells were recorded for each coded-aperture material composition and thickness investigated in this study. Three different W and ^{113}Cd compositions (25% W, 75% ^{113}Cd; 50% W, 50%^{113}Cd; 75% W, 25% ^{113}Cd) were examined. Based on the authors' initial study the thickness selected for testing was 25.4 mm [22].

4 Results

4.1 Comparison of the three scintillation samples

Three plastic scintillator samples were in turn exposed to the heavily-shielded ^{252}Cf fission source and their relative neutron and gamma-ray photon fluxes compared. The resulting plots against neutron and photon energy are presented in figure 4(a) and (b), respectively. A single simulation run consisted of 10^9 particle histories generated and particle flux in a cell was recorded for each scintillation sample. Uncertainty for each simulation run was below the confidence level of 0.05%.

Relative neutron and gamma-ray photon energy spectra measured from the unshielded fission spectrum of ^{252}Cf (figure 2(a)) can be compared to the results obtained for individual scintillator cell when the source energy is shielded through the water in the tank (figure 4(a)). While it can be observed that the measured neutron flux is greatly reduced, the neutron energy spectrum resembles the distribution of the unshielded source for all three samples.

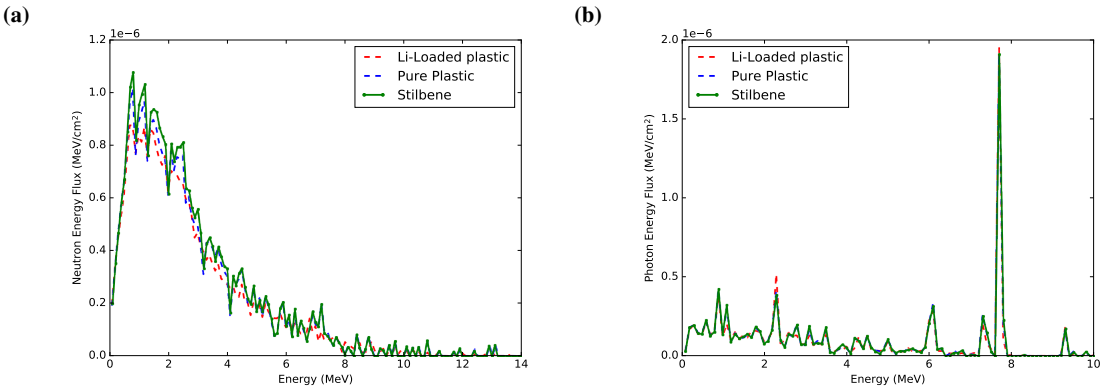

Figure 4. Relative particle fluxes for the three scintillator samples simulated and plotted against 100 keV energy bins for a) neutrons and b) gamma-ray photons.

2017 JINST 12 P12007

Gamma-ray photon spectrum of the unshielded source (figure 2(b)) on the other hand is significantly altered through the metal tank and Pb shielding provided (figure 4(b)). Based on the dissimilarity it can be concluded that most of gamma-ray photons produced by spontaneous fission ^{252}Cf have been successfully shielded by the Pb block located between the tank and the sensitive detector. The resulting peaks between 6–10 MeV are the result of neutron interactions with water in the tank, as well as neutron interactions with air around the detector, which are both accompanied by gamma release. There is also very little fluctuations between the photon flux measurements for different scintillators eliminating the scintillator from being the source of these species.

Additionally, the particle tracking card (PTRAC) was utilised to investigate 10^4 entries to the scintillator cell in order to estimate the highest neutron detection efficiency. Neutron interactions such as elastic scattering, inelastic scattering and capture events were recorded. The ^{252}Cf spontaneous fission source was defined as a point isotropic source, placed in a small Al capsule, as it is stored in real-life conditions at Lancaster University. The highest number of neutron interactions was recorded in the ^{6}Li-loaded plastic scintillator — 9905, which was followed by the single stilbene crystal — 8503 and the pure plastic sample — 8442. The highest neutron efficiency of the ^{6}Li-loaded sample is in this case associated with the loading of the scintillator, which allows thermal neutron detection due to high neutron absorption cross-section of the ^{6}Li. In this case, the plastic scintillator was loaded with 0.14% fractional mass of ^{6}Li.

The remaining 100–1500 interactions detected using PTRAC card within the scintillator cell were associated with gamma-ray induced Compton scattering events. Such results would suggest an unrealistic ratio between neutron and gamma-ray events detected. However, further investigation revealed that many thousands of neutron events detected within the scintillator do not originate in the ^{252}Cf source. In contrast to gamma-ray photons, which are successfully moderated through the Pb block and then further through the concrete walls of the neutron laboratory, neutrons are scattered by H molecules within the concrete walls. Hence, a large number of neutrons undergo elastic scattering interaction with H in the surrounding walls and can re-enter the scintillator cell, falsely increasing the number of neutron counts in the scintillator.

4.2 Coded-aperture optimisation

Neutron and photon flux measurements recorded for the individual cells of the sensitive detector have been utilised to investigate neutron blocking properties of the chosen material compositions as described in section 3. Total flux detected, as well as energy deposited, in a single detector cell were read via bespoke Matlab scripts to build a projection of the source, as seen through the coded-aperture. These unprocessed images were expected to closely reflect transparent and opaque elements of the coded-aperture pattern. For clarity the coded-aperture pattern exploited in this study is shown in figure 5, which is then further compared to the projections obtained.

Results of the relative neutron flux passing through a detector cell in figure 6 present a good resemblance of the pattern from figure 5. The central opaque horizontal line in figure 5 can be identified with a strip of low neutron flux crossing the projections around zero on the y-axis. Furthermore, the transparent elements of the pattern from figure 5 can be matched with the areas of the higher flux; the main vertical line crossing the images around zero on the x-axis. Although the three different compositions yield a very similar performance, the images presented in figure 6(i) and figure 6(j) claim the clearest separation between the areas of high and low neutron flux, which

2017 JINST 12 P12007

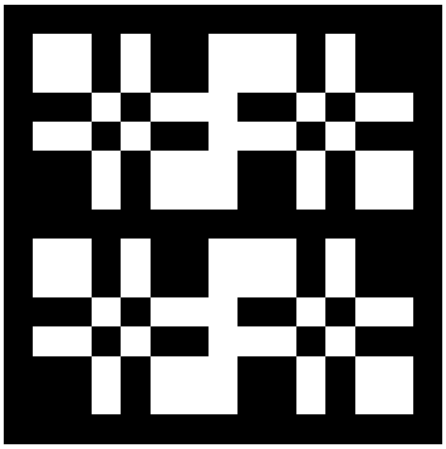

Figure 5. Rank 7 coded-aperture. Transparent and opaque elements are presented in white and black, respectively. With 84 transparent and 85 opaque elements, the modelled aperture yields 49.7% transparency. A frame of was added around the 13×13 aperture to represent clear boundaries. Reproduced from [22]. CC BY 3.0

is of vital importance when coded-aperture decoding algorithm is applied in order to obtain the location of the radiation source. Despite the difference in the neutron fluxes measured for the different radiation sources investigated, as evidenced by the difference of the colour intensity in figure 6, coded-aperture patterns are distinguishable for both simulated sources.

In a similar way, gamma-ray photon flux was measured in the sensitive detector (figure 7). As expected, the images reconstructed with regards to the gamma-ray flux passing through the sensitive detector show an even greater resemblance to the rank-7 coded-aperture pattern used. It is predominantly due to the very good gamma-ray shielding properties of the high Z element — W. It interacts with gamma-rays of energies up to approximately 1.5 MeV through Compton scattering and photoelectric effect. Hence, the difference between the modulation of the particle fields between ^{241}AmBe and ^{252}Cf is not as evident as for neutrons.

In addition to neutron and gamma-ray fluxes passing through a detector cell, energy deposition in a cell was also investigated. Pulse height tally (F8) scores in the detector's cells were mapped on to a square array to reconstruct the projections. In the case of neutron energy deposition (figure 6 columns 3 and 4), source reconstruction may be difficult due to unclear pictures, when contrasted with the coded-aperture pattern from figure 5. The vertical line of transparent elements crossing through the coded-aperture centre, which was easily identifiable in particle flux figures, can only be discerned with difficulty in energy deposition distributions. There is a tendency that can be observed across gamma-ray measurements, where the increase of W content in the composition is proportional to the increase of the projections' quality. Furthermore, there is a clear difference in particle modulation quality between the projections obtained in figure 7 (Columns 3 and 4) for ^{241}AmBe and ^{252}Cf. When compared with the corresponding results of gamma-ray flux measurement (figure 7 Columns 1 and 2) the quality of the image is significantly lower. It suggests that a large number of gamma-ray photons passes through the detector cells without depositing energy.

2017 JINST 12 P12007

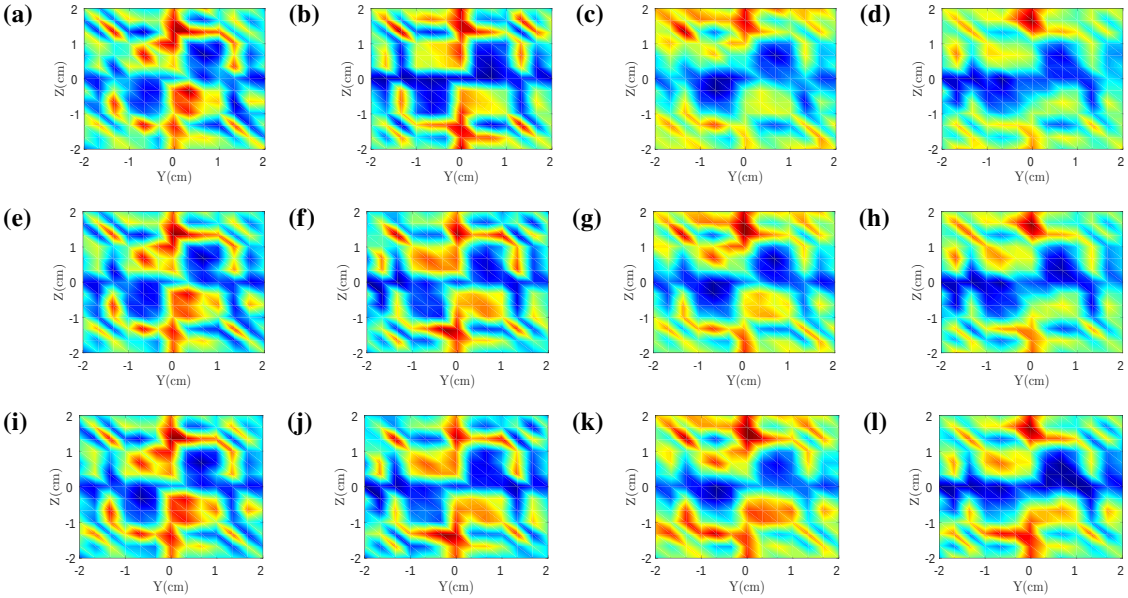

Figure 6. Neutron flux and energy deposition projected on the sensitive detector through the coded-aperture of three W-^{113}Cd compositions. Columns 1 and 2 shown neutron flux and columns 3 and 4 energy deposition for two different sources a) & c) W-25%, ^{113}Cd-75% with ^{241}AmBe b) & d) W-25%, ^{113}Cd-75% with ^{252}Cf e) & g) W-50%, ^{113}Cd-50% with ^{241}AmBe f) & (h) W-50%, ^{113}Cd-50% with ^{252}Cf i) & k) W-75%, ^{113}Cd-25% with ^{241}AmBe and j) & l) W-75%, ^{113}Cd-25% with ^{252}Cf. Intensity scale was normalised for all images to between $1e^{-7}$ and $1e^{-3}$ MeV/cm^2.

4.3 Source reconstruction

The results presented in the previous subsection were further processed via deconvolution algorithm implemented in a custom Matlab script. The process involves deconvolution of the input array (raw projections presented in the previous subsection) with the decoding array. It results in an array, whose expected outcome is a single impulse response, marking the location of the source. The decoding array is specific for a coded-aperture design of a set rank. Further details about the decoding process are presented here [22].

Reconstruction plots presented in figures 8, 9 show a good agreement with the results of the 'raw' data — before the decoding algorithm was applied. In the same way as the 'raw' data images, particle flux measurements (figure 6 and figure 7 Columns 1 and 2) present the most accurate exemplification of the location of the radiation source. Single hotspots can be clearly distinguished for neutron and gamma-ray images for both sources simulated. Moreover, the hotspot location in the middle of the reconstructed image claims 100% accuracy with the source coordinates specified as (0.0,0.0,0.0).

Images in figure 9 (Columns 3 and 4) present the source reconstruction based on the measurement of the energy deposition in a cell. A significant drop in the localisation accuracy, caused by the identification of multiple hotspots, is observed in many cases, with W-25%, ^{113}Cd-75% composition being mostly affected. There is also a general tendency that can be discerned across all the reconstructed images; the localisation accuracy is proportional to the increased W content in the composition. Furthermore, the images in figure 9 (Columns 3 and 4) suggest a considerably

2017 JINST 12 P12007

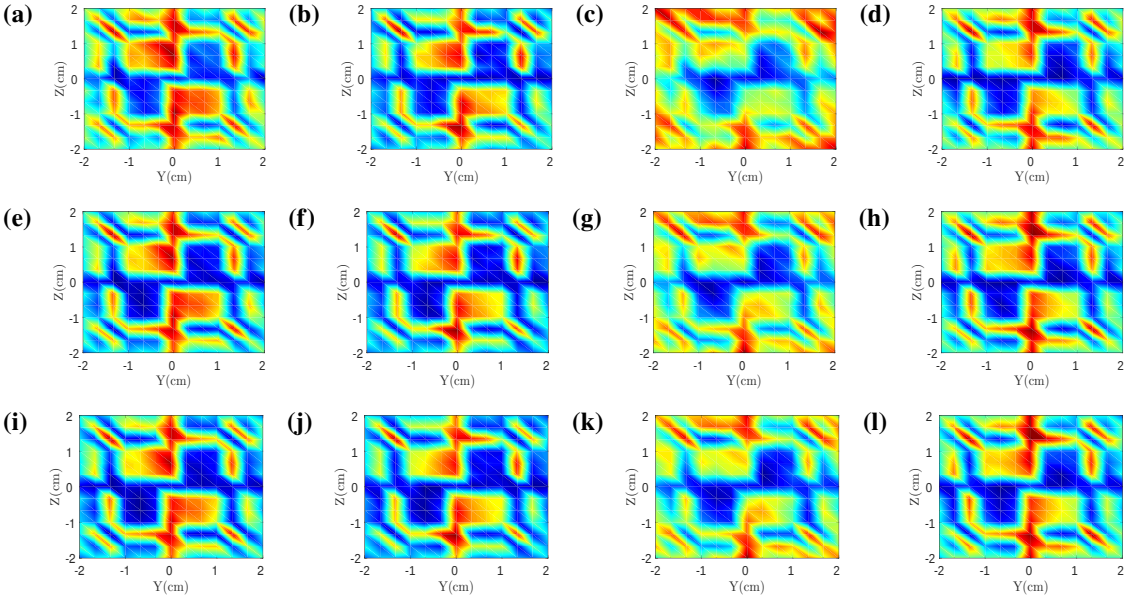

Figure 7. Gamma-ray photon flux and energy deposition projected on the sensitive detector through the coded-aperture of three W-^{113}Cd compositions. Columns 1 and 2 shown neutron flux and columns 3 and 4 energy deposition for two different sources a) & c) W-25%, ^{113}Cd-75% with ^{241}AmBe b) & d) W-25%, ^{113}Cd-75% with ^{252}Cf e) & g) W-50%, ^{113}Cd-50% with ^{241}AmBe f) & (h) W-50%, ^{113}Cd-50% with ^{252}Cf i) & k) W-75%, ^{113}Cd-25% with ^{241}AmBe and j) & l) W-75%, ^{113}Cd-25% with ^{252}Cf. Intensity scale was normalised for all images to between $1e^{-7}$ and $1e^{-3}$ MeV/cm^2.

greater detection accuracy for ^{252}Cf than for ^{241}AmBe.

5 Discussion

Based on the results presented in section 4.1 the most suitable candidate for the mixed-field imaging system for nuclear decommissioning applications would be the single stilbene crystal. Relative neutron energy flux measured was the highest in the crystal out of the three samples tested. The number of PTRAC interactions recorded, which was limited to 10,000 revealed that due to neutron capture events there were more neutron interactions in ^{6}Li-loaded plastic scintillator than in pure plastic or crystal. Devices used for mixed-field characterisation necessitate better neutron to gamma detection ratio, if these are to be used to simultaneously identify neutron and gamma-ray sources. Previous experimental study of ^{6}Li-loaded plastic scintillator shows good thermal neutron detection performance. However, it also reveals that fast neutrons and gamma-ray photons are difficult to separate using PSD with this scintillator, especially when exposed to ^{252}Cf field [32].

Another study investigating ^{6}Li-loaded plastic scintillators claims even better PSD separation performance [35]. In a similar way to Balmer et al. [32] Cherepy et al. [35] uses figure-of-merit (FOM) for PSD applications to estimate neutron/gamma separation performance of the scintillator [28]. The Cherepy et al. study claims the FOM of 1.4 in the 350 to 450 keVee energy range, which is approximately twice as high as in Balmer et al. The difference between the two studies lies most likely in the amount of ^{6}Li doping. Moreover, both of these experiments were performed

2017 JINST 12 P12007

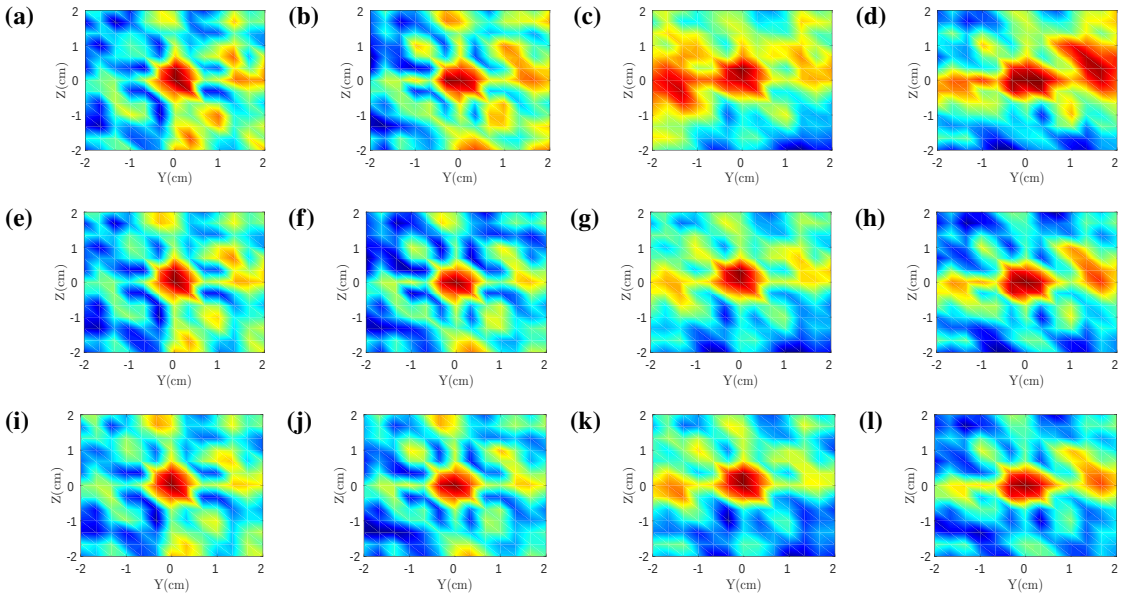

Figure 8. Neutron source reconstruction results based on particle flux measurements (Columns 1 and 2) and energy deposition (Columns 3 and 4) for W-^{113}Cd compositions a) & c) W-25%, ^{113}Cd-75% with ^{241}AmBe b) & d) W-25%, ^{113}Cd-75% with ^{252}Cf e) & g) W-50%, ^{113}Cd-50% with ^{241}AmBe f) & (h) W-50%, ^{113}Cd-50% with ^{252}Cf i) & k) W-75%, ^{113}Cd-25% with ^{241}AmBe and j) & l) W-75%, ^{113}Cd-25% with ^{252}Cf. Intensity scale was normalised for all images to between 1e^{-7} and 1e^{-3} MeV/cm^2.

in a controlled environment, enabling the neutrons from ^{252}Cf to be sufficiently thermalized for the neutron capture on ^{6}Li. However, authors' recent experimental study of the ^{6}Li-loaded scintillator shows that it fails to separate fast neutrons and gamma-ray photons from ^{252}Cf fission source, when the energy spectrum is modulated by means of water (in exactly the same way as simulated in this study) [36].

Furthermore, the absence of sufficient moderation (by means of Bonner Sphere or Polyethylene layer, as in the studies by Balmer et al. and Cherepy et al., respectively) relates to the lack of the peak resulting from ^{6}Li neutron capture interaction around 400 keVee in figure 4. Neutron energy spectrum from the heavily-shielded ^{252}Cf at Lancaster University peaks at approximately 0.7–0.9 MeV, as shown in figure 2(a). This is further supported by the aforementioned authors' experimental work, where thermal neutron peak was not detected and the ^{6}Li-loaded scintillator did not discriminate between neturons and gamma-ray photons at this energy level [36].

Although the single stilbene crystal presents the best neutron/gamma detection performance out of the three samples tested in this study its practical implementation can be prevented by the high manufacturing cost and little performance gain. Pure plastic scintillator sample shows only slightly inferior neutron/gamma detection performance, which relates to the neutron energy detection spectrum. Moreover, crystal scintillators are more susceptible to mechanical damage during transportation. Pure plastic scintillator such as EJ-299-34 does not only claim good PSD performance, even with relatively low neutron energy spectrum of ^{252}Cf but can also be machined to high precision for small imaging arrays [8, 26].

There is a general trend that can be observed across the results of the second part of the study.

2017 JINST 12 P12007

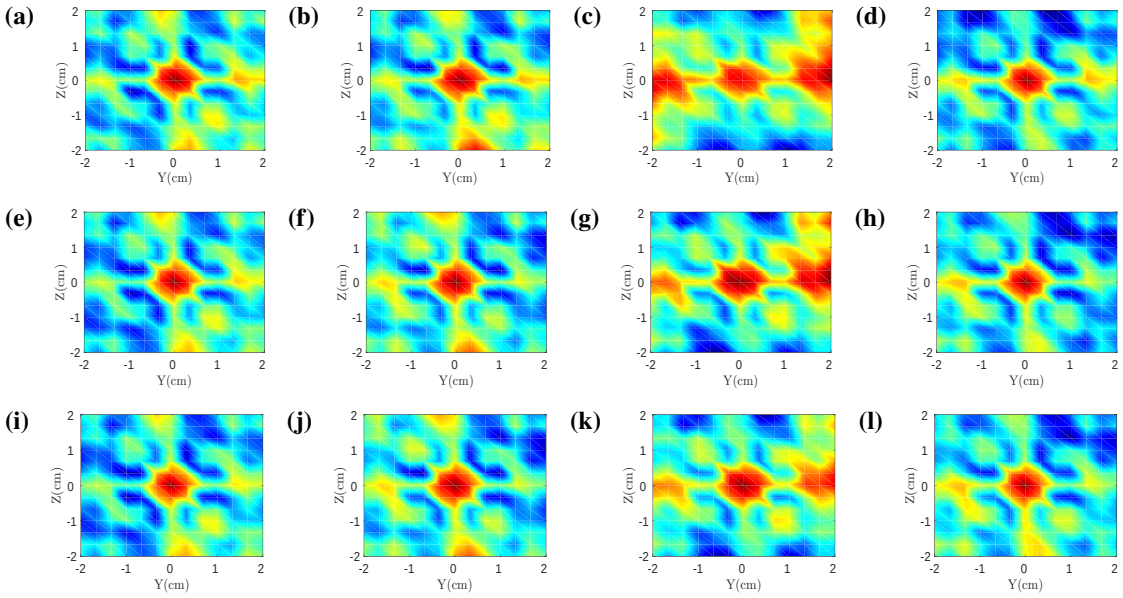

Figure 9. Gamma-ray source reconstruction results based on particle flux measurements (Columns 1 and 2) and energy deposition (Columns 3 and 4) for W-^{113}Cd compositions a) & c) W-25%, ^{113}Cd-75% with ^{241}AmBe b) & d) W-25%, ^{113}Cd-75% with ^{252}Cf e) & g) W-50%, ^{113}Cd-50% with ^{241}AmBe f) & (h) W-50%, ^{113}Cd-50% with ^{252}Cf i) & k) W-75%, ^{113}Cd-25% with ^{241}AmBe and j) & l) W-75%, ^{113}Cd-25% with ^{252}Cf. Intensity scale was normalised for all images to between $1e^{-7}$ and $1e^{-3}$ MeV/cm^2.

In all the cases considered the higher W content in the aperture material composition provides the most effective neutron/gamma field modulation. Thus, the W-75%, ^{113}Cd-25% composition offers the most accurate reconstruction of the simulated radiation source. However, the modulation performance of each material (and the source localisation as a result) is affected by the energy spectrum of the source.

With the average neutron energy spectrum of ^{241}AmBe higher than ^{252}Cf, the corresponding reconstructed source localisation images in figure 8 and figure 9 show greater intensity of the former. Despite the difference in the level of intensity, the localisation efficiency is comparable for both sources with only one clear neutron hotspot identified in the mentioned cases. There is a good agreement between the results based on neutron flux and energy deposited, as far as single hotspot identification is considered.

Gamma-ray source localisation on the other hand, is more efficient when particle flux is considered for the reconstruction. Figure 9 (Columns 1 and 2) presents an ideal source reconstruction with a single hotspot easily-identifiable in the centre of the image. In contrast, the energy deposited based images of ^{241}AmBe in figure 9 (Column 3) show poor source detection performance. In line with the previously made claim, the performance increases with the increased W content. This is observed due to a very high number of 4.4 MeV gamma-ray photons emitted form ^{241}AmBe. Therefore, the higher W content enables greater absorption of these gamma-rays in the aperture which in turn results in higher quality reconstruction. Nonetheless, multiple gamma-ray hotspots identified for ^{241}AmBe in figure 9 (Column 3) prevent reliable gamma-ray source detection and localisation. As the average gamma-ray spectrum of spontaneous fission ^{252}Cf source is much

2017 JINST 12 P12007

lower, even the lowest W content allows for the radiation source to be effectively reconstructed.

Based on the results presented the most suitable composition for the coded-aperture material would be W-75%, ^{113}Cd-25%. However, the W-50%, ^{113}Cd-50% composition claims only marginally inferior neutron/gamma field modulation performance. For practical application factors such as machining difficulty and the specific energy spectra would need to be considered. Since this study is aimed at mixed-field detection and characterisation of the radioactive sources with energy spectra similar to ^{252}Cf, one of the identified compositions could be considered for implementation.

Acknowledgments

The authors would like to acknowledge the funding support from EPSRC (grant number EP/M507891/1) via Faculty of Science and Technology, Lancaster University, U.K. and Sellafield Ltd. We also acknowledge the help and advice of Dr Matthew Balmer and Mr Mauro Licata at Lancaster University, U.K. The authors acknowledge the use of SimpleGeo visualisation program and the Matplotlib package in this research [37, 38].

References

[1] T. Szczesniak et al., *Light pulse shapes in liquid scintillators originating from gamma-rays and neutrons*, *IEEE Trans. Nucl. Sci.* **57** (2010) 3846.

[2] K.A.A. Gamage, M.J. Joyce and G.C. Taylor, *A digital approach to neutron-γ imaging with a narrow tungsten collimator aperture and a fast organic liquid scintillator detector*, *Appl. Radiat. Isot.* **70** (2012) 1223.

[3] A. Kaplan, M. Flaska, A. Enqvist, J. Dolan and S. Pozzi, *EJ-309 pulse shape discrimination performance with a high gamma-ray-to-neutron ratio and low threshold*, *Nucl. Instrum. Meth.* **A 729** (2013) 463.

[4] A. Jones and M. Joyce, *The angular dependence of pulse shape discrimination and detection sensitivity in cylindrical and cubic EJ-309 organic liquid scintillators*, 2017 *JINST* **12** T01005.

[5] F. Brooks, *A scintillation counter with neutron and gamma-ray discriminators*, *Nucl. Instrum. Meth.* **4** (1959) 151.

[6] K. Gamage and G. Taylor, *Neutron gamma fraction imaging: Detection, location and identification of neutron sources*, *Nucl. Instrum. Meth.* **A 788** (2015) 9.

[7] G. Hull et al., *New organic crystals for pulse shape discrimination*, *IEEE Trans. Nucl. Sci.* **56** (2009) 899.

[8] N. Zaitseva et al., *Plastic scintillators with efficient neutron/gamma pulse shape discrimination*, *Nucl. Instrum. Meth.* **A 668** (2012) 88.

[9] Eljen Technology, *Neutron/Gamma PSD Liquid Scintillator EJ-301,EJ-309*, http://www.eljentechnology.com/images/products/data_sheets/EJ-301_EJ-309.pdf (2016).

[10] M. Bourne, S. Clarke, N. Adamowicz, S. Pozzi, N. Zaitseva and L. Carman, *Neutron detection in a high-gamma field using solution-grown stilbene*, *Nucl. Instrum. Meth.* **A 806** (2016) 348.

[11] D.B. Pelowitz, *MCNPX USER'S MANUAL — Version 2.7.0* (2011).

2017 JINST 12 P12007

[12] M. Gerrit et al., *Organic liquid scintillation detectors for on-the-fly neutron / gamma alarming and radionuclide identification in a pedestrian radiation portal monitor*, *Nucl. Instrum. Meth.* **A 789** (2015) 16.

[13] A. Poitrasson-rivière et al., *Angular-resolution and material-characterization measurements for a dual-particle imaging system with mixed-oxide fuel*, *Nucl. Instrum. Meth.* **A 797** (2015) 278.

[14] J.S. Beaumont, B.A. Shippen, M.P. Mellor and M.J. Joyce, *Imaging of fast neutrons and gamma rays from environment Cf in a heavily shielded*, *Nucl. Instrum. Meth.* **A 847** (2017) 77.

[15] P. Besson et al., *CARTOGAM: a portable gamma camera*, *Nucl. Instrum. Meth.* **A 387** (1997) 297.

[16] S.V. Guru et al., *Portable high energy gamma ray imagers*, *Nucl. Instrum. Meth.* **A 378** (1996) 612.

[17] J. Beaumont, B. Colling, M.P. Mellor and M.J. Joyce, *On the design and test of a neutron collimator for real-time neutron imaging in the mev energy range*, in *2013 3rd International Conference on Advancements in Nuclear Instrumentation, Measurement Methods and their Applications (ANIMMA)*, Piscataway, U.S.A. (2013), pg. 1.

[18] E.E. Fenimore and T.M. Cannon, *Coded aperture imaging with uniformly redundant arrays*, *Appl. Optics* **17** (1978) 337.

[19] S.R. Gottesman and E.E. Fenimore, *New family of binary arrays for coded aperture imaging*, *Appl. Optics* **28** (1989) 4344.

[20] E. Del Monte et al., *An X-ray imager based on silicon microstrip detector and coded mask*, *Nucl. Instrum. Meth.* **A 576** (2007) 191.

[21] R. Accorsi and R.C. Lanza, *Near-field artifact reduction in planar coded aperture imaging*, *Appl. Optics* **40** (2001) 4697.

[22] M. J. Cieślak, K.A. Gamage and R. Glover, *Coded-aperture imaging systems: Past, present and future development – A review*, *Radiat. Meas.* **92** (2016) 59.

[23] P. Marleau, J. Brennan, E. Brubaker and J. Steele, *Results from the coded aperture neutron imaging system*, *IEEE Nucl. Sci. Symp. Med. Imag.* **2010** (2010) 1640.

[24] R.S. Woolf, B.F. Phlips, A.L. Hutcheson and E.A. Wulf, *Fast-neutron, coded-aperture imager*, *Nucl. Instrum. Meth.* **784** (2015) 398.

[25] P. Hausladen, J. Newby, F. Liang and M. Blackston, *The Deployable Fast-Neutron Coded- Aperture Imager: Demonstration of Locating One or More Sources in Three Dimensions*, https://info.ornl.gov/sites/publications/Files/Pub46191.pdf.

[26] Eljen Technology, *Neutron/Gamma PSD Plastic Scintillator EJ-276 (formerly EJ-299-33A and EJ-299-34)*, http://www.eljentechnology.com/images/products/data_sheets/EJ-276.pdf (2017).

[27] Hamamatsu Photonics, *Flat Panel Type Multianode Photomultiplier Tube Assembly H9500, H9500-03*, https://www.hamamatsu.com/resources/pdf/etd/H9500_H9500-03_TPMH1309E.pdf (2015).

[28] G.F. Knoll, *Radiation Detection and Measurement*, fourth edition, John Wiley & Sons, Hoboken U.S.A. (2010).

[29] T.E. Valentine, *Evaluation of prompt fission γ rays for use in simulating nuclear safeguard measurements*, http://citeseerx.ist.psu.edu/viewdoc/download?doi=10.1.1.559.8358&rep=rep1&type=pdf (1999).

[30] R. Gehrke, R. Aryaeinejad, J. Hartwell, W. Yoon, E. Reber, J. Davidson, *The γ-ray spectrum of 252Cf and the information contained within it*, *Nucl. Instrum. Meth.* **B 213** (2004) 10.

2017 JINST 12 P12007

[31] Inrad Optics, Stilbene Single Crystals, Data sheet, http://www.inradoptics.com/products/scintillation-crystals.

[32] M.J. Balmer, K.A. Gamage and G.C. Taylor, *Comparative analysis of pulse shape discrimination methods in a 6Li-loaded plastic scintillator*, *Nucl. Instrum. Meth.* **A 788** (2015) 146.

[33] M. Gmar, M. Agelou, F. Carrel and V. Shoepff, *GAMPIX: A new generation of gamma camera*, *Nucl. Instrum. Meth.* **A 652** (2011) 638.

[34] Y. Wu, J. Song, H. Zheng, G. Sun, L. Hao, P. Long and L. Hu, *CAD-based Monte Carlo program for integrated simulation of nuclear system SuperMC*, *Ann. Nucl. Energy* **82** (2015) 161.

[35] N.J. Cherepy et al., *Bismuth- and lithium-loaded plastic scintillators for gamma and neutron detection*, *Nucl. Instrum. Meth.* **A 778** (2015) 126.

[36] M.J. Cieślak, K.A.A. Gamage and R. Glover, *Pulse shape discrimination characteristics of stilbene crystal, pure and 6Li loaded plastic scintillators for a high resolution coded-aperture neutron imager*, 2017 *JINST* **12** P07023.

[37] C. Theis et al., *Interactive three-dimensional visualization and creation of geometries for Monte Carlo calculations*, *Nucl. Instrum. Meth.* **A 562** (2006) 827.

[38] J.D. Hunter, *Matplotlib: A 2D Graphics Environment*, *Comput. Sci. Engin.* **9** (2007) 90.

2017 JINST 12 P12007